2010 IEEE International Conference on Robotics and Automation
Anchorage Convention District
May 3-8, 2010, Anchorage, Alaska, USA

Implementation of a 4-DOF Parallel Mechanism as a Needle Insertion Device

Jaeheon Chung, Hyo-Jeong Cha, Byung-Ju Yi, *Member, IEEE* and Whee Kuk Kim, *Member, IEEE*

***Abstract*—Recently, quite a few practical parallel mechanisms having spatial 3-DOF and 6-DOF have been introduced and implemented. However, not many useful practical applications using low-mobility parallel mechanisms having 4-DOF and 5-DOF have been developed. In this paper, we propose a 4-DOF parallel mechanism for needle insertion application in which proper orientation and needle insertion process are required. The mechanism has four outer chains and one passive middle chain through which a needle insertion motion occurs. The kinematic modeling and kinematic analysis are performed to understand the characteristics of this mechanism. Through the singularity analysis, a singularity-free design for the desired workspace is proposed. Finally, the effectiveness of this device as a needle insertion device is shown through experimental work.**

I. Introduction

RECENTLY, low-mobility parallel mechanisms have drawn attention due to their potential usefulness for many applications that require less degrees of freedom such as 4 or 5 degrees of freedom (DOF). In fact, there have been many elegant low-mobility parallel mechanisms suggested so far [1-4] but only small portion of them such as many 4-DOF robots based on Delta-robot concept have been proven for their excellent performance in practical applications [2, 3]. Along with these application oriented researches, lots of efforts have been made on type synthesis for such low-mobility mechanisms. As a result, numerous promising mechanism structures have been suggested [5-11]. However, most of these works have been focused on suggesting feasible structures of low-mobility parallel mechanisms.

There has been drastic progress reported in medical robotic systems in past decades. Particularly, there have been many previous works related to needle insertion tasks. One- or two-DOF needle insertion devices have been tested for the needle insertion or steering tests [12-14]. However, they are not adequate to perform the needle insertion task requiring more motion degrees of freedom. On the other hand, Fichtinger *et al*. [15] and Masamune *et al*. [16] proposed serial type needle placement devices that have more than six degrees of freedom. They belong to typical serial type of needle insertion devices and are classified as floating needle insertion devices in that they are attached to the end of a medical robot generating a gross motion. Note that a well-known da Vinci surgical system [17] employs a similar design concept. However, stiffness for this type of serial structured needle insertion devices is relatively low and thus its accuracy is relatively low due to its cantilever structure. Thus they are not suitable for tasks requiring very high precision or for tasks under external disturbances.

In fact, the needle insertion task is required in various surgical procedures. As an exemplary application, a needle insertion task for a specified insertion position is sketched roughly in Fig. 1. It can be easily seen from the figure that the required motions are 4-DOF; 1-DOF translational motion for the needle insertion, 2-DOF tilting motion for the needle pose, and 1-DOF rotational motion for the needle steering. A new design to effectively conduct such needle insertion task could enhance the accuracy of the needle insertion operation. Desired features for those needle insertion devices could be summarized as follows: *i*) it could be accurate and stiff, *ii*) it should be compact to be used together with a variety of other medical equipments, and *iii*) and it should have the 4-DOFs. In addition, a path guider for the needle may be required to tightly hold the insertion pose during the medical treatment. In short, a candidate adequate to meet all these requirements would be a compact 4-DOF parallel mechanism with a path guider.

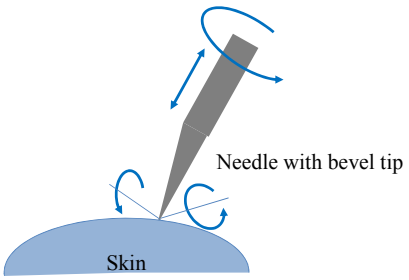

Fig. 1. The required motions for a needle insertion task.

Thus, in this work, a 4-DOF parallel mechanism is

This work was partially supported by the Korea Science and Engineering Foundation (KOSEF) grant funded by the Korea government (R01-2008-000-11742-0), partially supported by the GRRC program of Gyeonggi province (2008-041-0003 -0001), partially supported by the Ministry of Knowledge Economy (MKE) and Korea Industrial Technology Foundation (KOTEF) through the Human Resource Training Project for Strategic Technology, and the outcome of a Manpower Development Program for Energy & Resources supported by the Ministry of Knowledge and Economy (MKE).

J. Chung is with the Department of Advanced Medical Initiatives, Faculty of Medical Sciences, Kyushu University, Fukuoka, Japan. (e-mail:jaeheon.chung@gmail.com)

H.-J. Cha is with the School of Electrical Engineering and Computer Science, Hanyang University, Ansan, Korea. (e-mail: chacne@nate.com).

B.-J. Yi is with the School of Electrical Engineering and Computer Science, Hanyang University, Ansan, Korea. (corresponding author phone: +82-31-400-5218; fax: +82-31-416-6416; e-mail: bj@ hanyang.ac.kr).

W. K. Kim is with the Department of Control and Instrumentation Engineering, Korea University, Korea. (e-mail:wheekuk@korea.ac.kr).

proposed which is compact and attachable to skin, and has a path guider for the needle. Fig. 2 shows the 3D-model of the proposed needle insertion device which has 4-DOF motion and a path guider. Fig. 3 shows the concept of a medical application using the proposed parallel mechanism as the needle insertion device. This procedure consists of three stages. First, the needle insertion device is fixed to the surface of skin. Next, the user determines the pose of the needle. Finally, the needle is inserted into the skin. Additional needle insertion can be done by the user or an automatic insertion device.

The contents of this work are summarized as follows. In section II, the kinematic model is described and the kinematic analysis is performed in section III. Singularity analysis for the proposed mechanism is conducted in section IV. Implementation and experimentation of the mechanism is performed in section V. Finally, section VI draws the conclusion.

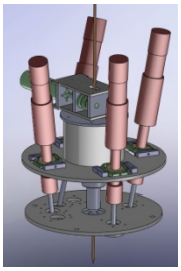

Fig. 2. The 3D-model for the needle insertion device.

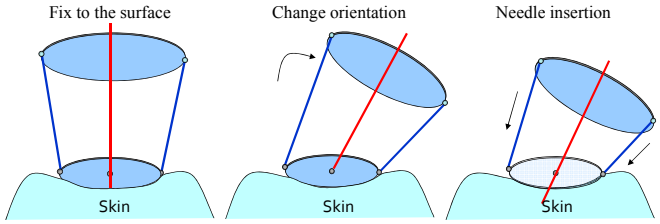

Fig. 3. The concept of the needle insertion procedure

II. KINEMATICS

A. Description of the Mechanism

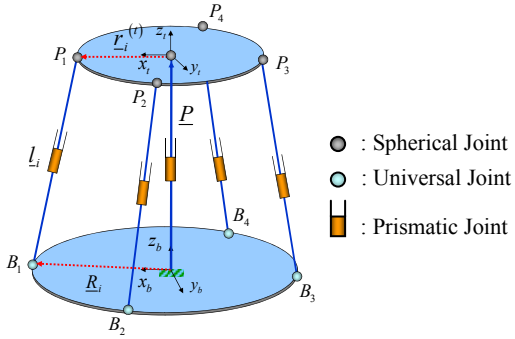

Fig. 4 The description of the mechanism.

Figure 4 shows the kinematic description of this mechanism. It consists of a top plate, a base plate, four external legs with UPS (universal, prismatic, and spherical) structure and one internal leg with PS (prismatic and spherical) structure connecting those two plates. The mobility of this mechanism can be easily confirmed to be 4 from the well-known Grübler's mobility formula.

The origin of the base frame $\{\hat{x}_b, \hat{y}_b, \hat{z}_b\}$ and one of the output frame $\{\hat{x}_t, \hat{y}_t, \hat{z}_t\}$ is located at the center of the base plate and the top plate, respectively, as shown in Fig. 4. Denote $\underline{P} = [x_t \quad y_t \quad z_t]^T$ as the position vector from the origin of the base frame to the origin of the output frame. Since the mechanism is constrained by an internal leg not to move in the x- and y- directions, the output position vector can be expressed as $(x_0 \; y_0 \; z)^T$, where the positions x_0 and y_0 are fixed values and only the position z is a variable. And denote the points B_i and P_i as the locations where a universal joint and a spherical joint of the i^{th} external leg is placed, respectively. The position vector from the point B_i to the point P_i is denoted as $\underline{l}_i$. And the offset angles which represent the locations of the corresponding joints on the base plate and the top plate is denoted as μ_a and μ_b, respectively, as shown in Fig. 5.

$\underline{R}_i$ represents the position vector from the origin of the base plate to the universal joint of the i^{th} external leg with respect to the base frame and $\underline{r}_i^{(t)}$ represents the position vector from the origin of the top plate to the spherical joint of the i^{th} external leg with respect to the top frame.

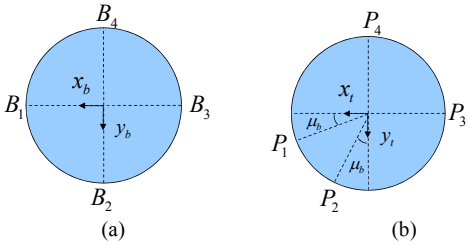

Fig. 5. Base and top plate. (a) Base plate. (b) Top plate.

B. Inverse Kinematics

Inverse kinematics is to find the input vector when the output position/orientation vector of the mechanism is given. Using the $x-y-z$ Euler angle set, the rotation matrix $[R_b^t]$ of the output frame is denoted as

$$[R_b^t] = [Rot(\mathbf{x}, \alpha)][Rot(\mathbf{y}, \beta)][Rot(\mathbf{z}, \gamma)] \quad (1)$$

where $Rot(\mathbf{x}, \alpha)$ denotes the rotation about the x-axis by α degree.

Now, the position vector $\underline{l}_i$ in terms of the i^{th} external leg can be expressed as

$$\underline{l}_i = \underline{P} + \underline{r}_i - \underline{R}_i, \text{ for } i=1, 2, 3, 4 \quad (2)$$

where

$$\underline{r}_i = [R_b^t]\underline{r}_i^{(t)}. \quad (3)$$

The displacement of the input joint variable l_i can be obtained by taking inner product of itself as follows

$$\underline{l}_i \bullet \underline{l}_i = l_i^2 = \left(\underline{P} + \underline{r}_i - \underline{R}_i\right) \bullet \left(\underline{P} + \underline{r}_i - \underline{R}_i\right). \quad (4)$$

C. First-order Kinematics

To obtain the velocity relation between the input joint vector and the independent output vector, the first-order kinematics for each of five legs (namely four external legs and an internal leg) are used. Firstly, the first order kinematics of the external legs can be obtained in the following way. Assume that input joints are located at the prismatic joints of all external legs. Then, the first-order kinematics of the external legs can be obtained by directly differentiating (4) respect to time as follows.

$$l_i \dot{l}_i = \dot{\underline{P}} \bullet \left(\underline{P} + \underline{r}_i - \underline{R}_i\right) + \dot{\underline{r}}_i \bullet \left(\underline{P} + \underline{r}_i - \underline{R}_i\right) \quad (5)$$

and

$$l_i \dot{l}_i = \underline{l}_i \bullet \dot{\underline{P}} + \left(\underline{r}_i \times \underline{l}_i\right) \bullet \underline{\omega} \quad (6)$$

where $\dot{\underline{P}}$ and $\underline{\omega}$ denote the linear velocity vector and the angular velocity vector of the output frame (the top plate), respectively.

Now, (6) can be expressed in a matrix form as

$$[A]\begin{bmatrix} \dot{\underline{P}} \\ \underline{\omega} \end{bmatrix} = [B]\begin{bmatrix} \dot{l}_1 \\ \dot{l}_2 \\ \dot{l}_3 \\ \dot{l}_4 \end{bmatrix} \quad (7)$$

where

$$[A] = \begin{bmatrix} \underline{l}_1^T & \left(\underline{r}_1 \times \underline{l}_1\right)^T \\ \underline{l}_2^T & \left(\underline{r}_2 \times \underline{l}_2\right)^T \\ \underline{l}_3^T & \left(\underline{r}_3 \times \underline{l}_3\right)^T \\ \underline{l}_4^T & \left(\underline{r}_4 \times \underline{l}_4\right)^T \end{bmatrix}, \quad [B] = \begin{bmatrix} l_1 & 0 & 0 & 0 \\ 0 & l_2 & 0 & 0 \\ 0 & 0 & l_3 & 0 \\ 0 & 0 & 0 & l_4 \end{bmatrix}, \quad (8)$$

$$\dot{\underline{u}} = \begin{bmatrix} \dot{\underline{P}}^T & \underline{\omega}^T \end{bmatrix}^T, \qquad \dot{\underline{\phi}}_a = \begin{bmatrix} \dot{l}_1 & \dot{l}_2 & \dot{l}_3 & \dot{l}_4 \end{bmatrix}^T.$$

Here, $\dot{\underline{\phi}}_a$ and $\dot{\underline{u}}$ denote the joint velocity vector and the output velocity vector, respectively. The relationship between the joint velocity vector and the output velocity vector can be found by pre-multiplying $[B]^{-1}$ to both sides of (7) as

$$\dot{\underline{\phi}}_a = \left[G_u^a\right]\begin{bmatrix} \dot{\underline{P}} \\ \underline{\omega} \end{bmatrix} = \left[G_u^a\right]\dot{\underline{u}} \quad (9)$$

where

$$\left[G_u^a\right] = [B]^{-1}[A]. \quad (10)$$

Secondly, the first-order kinematics of the internal chain can be obtained as

$$\dot{\underline{u}} = \begin{bmatrix} 0 & 0 & 0 & 0 \\ 0 & 0 & 0 & 0 \\ 1 & 0 & 0 & 0 \\ 0 & 1 & 0 & s_{i3} \\ 0 & 0 & c_{i2} & -s_{i2}c_{i3} \\ 0 & 0 & s_{i2} & c_{i2}c_{i3} \end{bmatrix} \dot{\underline{\phi}}_I = \left[G_{\phi_I}^u\right]\dot{\underline{\phi}}_I \quad (11)$$

where $\dot{\underline{\phi}}_I$ denotes the joint velocity vector of the internal chain, and $\left[G_{\phi_I}^u\right]$ denotes Jacobian between the output velocity vector $\dot{\underline{u}}$ and $\dot{\underline{\phi}}_I$. The output velocity $\dot{\underline{u}}$ of (11) can be divided into the independent and dependent output vectors as below

$$\dot{\underline{u}} = \begin{bmatrix} \dot{\underline{u}}_p \\ \dot{\underline{u}}_I \end{bmatrix} = \left[G_{\phi_I}^u\right]\dot{\underline{\phi}}_I = \begin{bmatrix} \left[G_{\phi_I}^{u_P}\right] \\ \left[G_{\phi_I}^{u_I}\right] \end{bmatrix}\dot{\underline{\phi}}_I \quad (12)$$

where $\dot{\underline{u}}_p = \begin{bmatrix} \dot{x} & \dot{y} \end{bmatrix}^T$ and $\dot{\underline{u}}_I = \begin{bmatrix} \dot{z} & \omega_x & \omega_y & \omega_z \end{bmatrix}^T$ denote the dependent and independent set of the output velocity vector, respectively. Finally, by inserting (11) into the external Jacobian matrix of (9) the first-order internal kinematics of the mechanism representing the relation between independent joint vector and the dependent joint vector can be obtained.

From (12), the relation between the dependent output velocity vector ($\dot{\underline{u}}_P$) and the independent output velocity vector ($\dot{\underline{u}}_I$) can be extracted as follows

$$\dot{\underline{u}}_p = \left[G_{\phi_I}^{u_P}\right]\left[G_{\phi_I}^{u_I}\right]^{-1}\dot{\underline{u}}_I = \left[G_{u_I}^{u_P}\right]\dot{\underline{u}}_I. \quad (13)$$

Thus, the relation between the output velocity ($\dot{\underline{u}}$) and the independent output velocity vector can be expressed as

$$\dot{\underline{u}} = \begin{bmatrix} \dot{\underline{u}}_I \\ \dot{\underline{u}}_P \end{bmatrix} = \begin{bmatrix} I_{4\times 4} \\ \left[G_{u_I}^{u_P}\right] \end{bmatrix}\dot{\underline{u}}_I = \left[G_{u_I}^u\right]\dot{\underline{u}}_I \quad (14)$$

where $I_{4\times 4}$ denotes an 4 by 4 identity matrix. Substituting (14) into (9), we have

$$\dot{\underline{\phi}}_a = \left[G_{u_I}^a\right]\dot{\underline{u}}_I \quad (15)$$

where $\left[G_{u_I}^a\right] \in R^{4\times 4}$ can be expressed as

$$\left[G_{u_I}^a\right] = \left[G_u^a\right]\left[G_{u_I}^u\right]. \quad (16)$$

Finally, the first-order kinematic relation between the independent output vector and the input joint vector can be obtained as follows

$$\dot{\underline{u}}_I = \left[G_a^{u_I}\right]\dot{\underline{\phi}}_a \quad (17)$$

where $\left[G_a^{u_I}\right] = \left[G_{u_I}^a\right]^{-1} \in R^{4\times 4}$.

III. Kinematic Analysis

Two design indices are considered to measure the kinematic characteristics of the proposed 4-DOF parallel mechanism.

TABLE I
KINEMATIC PARAMETERS

Parameter	R	R	L_b
Length	0.045[m]	0.036[m]	0.041[m]

Table I shows link parameters used in simulation. R, r, and L_b denote the radius of the base plate, the radius of the top plate, and a constant link length (i.e., the minimum stroke of the prismatic joint) of the prismatic joint, respectively. The maximum stroke of the prismatic joint is 0.058m.

A. Workspace

One of the basic aspects in robot design is to determine the workspace. In this analysis, the volume of reachable workspace is defined as

$$V = \int_V dV. \tag{18}$$

Figure 6 shows the reachable workspace for the case of $\gamma = 0^\circ$ (γ : a roll angle with respect to the local z-axis of the top plate). From this plot, it can be seen that the workspace size around the center of the workspace is fairly large. Through simulation for other values of γ, it can be confirmed that the mechanism ensures large workspace with respect to the roll angle γ.

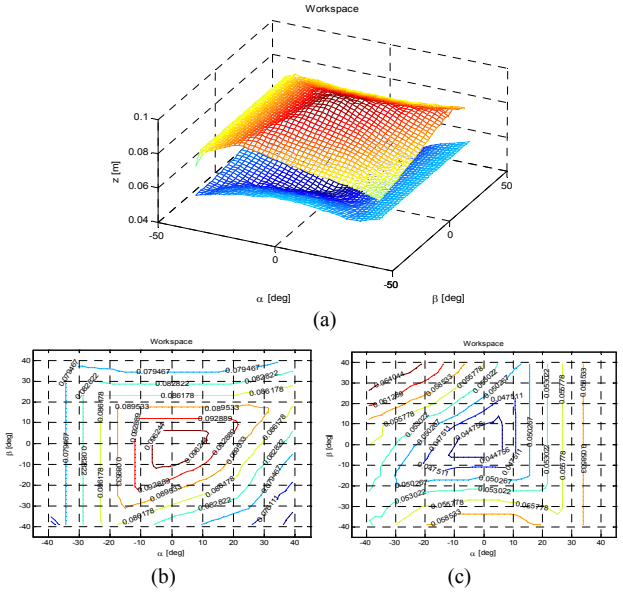

Fig. 6. Workspace. (a) 3-D plot. (b) Contour plot of α and β with respect to z max. (c) Contour plot of α and β with respect to z min.

B. Isotropic Index

The kinematic isotropic index is defined as

$$\sigma_I = \frac{\sigma_{\min}\left(\left[G_a^{u_I}\right]\right)}{\sigma_{\max}\left(\left[G_a^{u_I}\right]\right)} \tag{19}$$

where $\sigma_{\min}$ and $\sigma_{\max}$ denotes the minimum and the maximum singular value of $\left[G_a^{u_I}\right]$, respectively. When σ_I becomes unity, the end-effecter can generate uniform velocity in all directions.

Figure 7 shows the 3-D plot and the contour plot of the isotropic index, with respect to two orientation angles α and β, for the fixed values of z=0.07m and $\gamma = 0^\circ$ when the offset angles of both base and top platforms are symmetrically placed 90° apart one another. However, it is noted that when the offset angles (μ_a and μ_b) in both base and top plates are zero such as Fig. 5(a), values of the isotropic index are close to zero along the cross lines passing through the center of the workspace. Obviously, locations of these singular configurations in the middle of workspace are not desirable. However, it can be observed that when an offset angle (μ_b) of the top plate is adjusted while fixing the offset angles on the base plate, the singular region tends to move from the center region of the workspace to its boundary region as shown in Fig. 8.

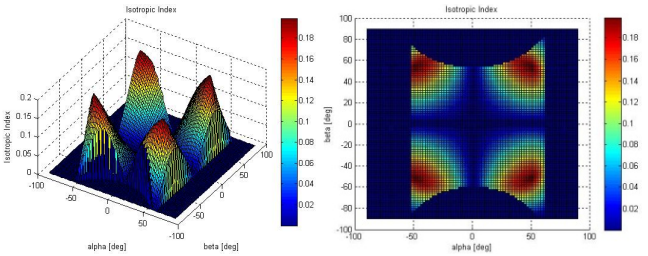

Fig. 7. Isotropic index when z=0.07m, $\mu_a = 0^\circ$ and $\mu_b = 0^\circ$. (a) Oblique view. (b) Top view.

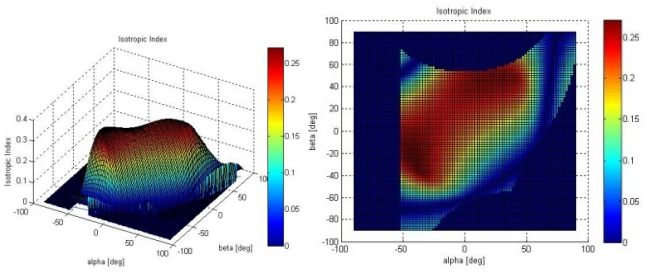

Fig. 8. Isotropic index when z=0.07m, $\mu_a = 0^\circ$ and $\mu_b = 30^\circ$. (a) Oblique view. (b) Top view.

IV. Singularity Analysis

In this section, forward kinematic singularity and inverse kinematic singularity of the proposed mechanism are investigated. Generally, these singularities can be found from the following equation [18].

$$A_u \underline{\dot{u}} = B_\phi \underline{\dot{\phi}} \tag{20}$$

which is equivalent to (7). Here, when the determinant of the A_u matrix is zero, the forward kinematic singularity occurs. When the determinant of the matrix B_ϕ is zero, the inverse kinematic singularity occurs. However, the inverse kinematic singularity does not exist because in (16) the components of the matrix B_ϕ are all constant values. On the other hand, the forward kinematic singularity of the mechanism could be identified by imposing the condition that the determinant of the matrix $[A]$ of (7) becomes zero. However, it is not straightforward to clearly identify this kind of singularity in an algebraic way. Thus, we employ Grassmann geometric method [19, 20] to identify the forward singularity as follows.

Note that there are two constraints imposed on the moving plate by locating a PS type sub-chain in the middle of the mechanism. They are given as

$$v_x = 0,\ v_y = 0. \tag{21}$$

When these two constraints are embedded into (7), the full first-order kinematic velocity equation of the mechanism can be formed as

$$[A_f]\begin{bmatrix}\boldsymbol{v}\\ \boldsymbol{\omega}\end{bmatrix}=[B_f]\dot{\boldsymbol{\theta}}_a \tag{22}$$

where

$$[A_f]=\begin{bmatrix} \underline{l}_1^T & (\underline{r}_1\times\underline{l}_1)^T\\ \underline{l}_2^T & (\underline{r}_2\times\underline{l}_2)^T\\ \underline{l}_3^T & (\underline{r}_3\times\underline{l}_3)^T\\ \underline{l}_4^T & (\underline{r}_4\times\underline{l}_4)^T\\ 1\ 0\ 0 & \mathbf{0}_{1\times3}\\ 0\ 1\ 0 & \mathbf{0}_{1\times3}\end{bmatrix},\ [B_f]=\begin{bmatrix}[B] & [\mathbf{0}]_{4\times1} & [\mathbf{0}]_{4\times1}\\ [\mathbf{0}]_{1\times4} & 0 & 0\\ [\mathbf{0}]_{1\times4} & 0 & 0\end{bmatrix}. \tag{23}$$

Note that the first through fourth rows of $[A_f]$ represent lines (plücker coordinates) with respect to the reference frame defined at the center of the moving plate, and also that the fifth and sixth rows of $[A_f]$ represent lines passing through the origin of the reference frame.

Now, we consider the cases when the variety formed with six rows of $[A_f]$ (or six lines) degenerates.

Case 1) When the moving plate coincides with the base plate, two lines representing the fifth and the sixth rows of $[A_f]$ also lie on the same plane. In this configuration, all lines are coplanar and thus the dimension of variety for all six lines degenerates to three: more specifically, all six lines span 2-DOF translational motion space and 1-DOF rotational motion space. Noting, however, that these 2-DOF translational motion space coincides with the constraint space imposed by the fifth and sixth rows of $[A_f]$, only 1-DOF rotational motion is feasible and controllable by input joints. Fig. 9(a) shows this case.

Case 2) When all lines are coplanar and intersect at the center of the base frame, the dimension of variety degenerates to 2: all lines span 2-DOF translational motion space. Again noting that these 2-DOF translational motions represent constraints, any 4-DOF motion of the mechanism is not controllable by input joints. Fig. 9(b) corresponds to this case.

Case 3) When any two lines out of the first four rows of $[A_f]$ pass through the center of the moving plate, the dimension of variety for those four lines degenerates to3. It can be easily seen that about the center of the moving plate only two line vectors are available to generate rotational motions and the other two lines could generate a translational motion along the z axis. Thus, the feasible motion of the mechanism could be 3-DOF motion at most, a 1-DOF translational motion along the z direction and 2-DOF rotational motions, and Fig. 9(c) shows a feasible configuration. Thus, the one rotational degree of freedom of the mechanism cannot be controlled in this configuration.

Case 4) When upper four lines of $[A_f]$ intersect at a common point as shown in Fig. 9(d), the dimension of variety for those four lines degenerates to 3. In this situation, the translational motion along the z axis is controllable, but the rotational motion of the mechanism is not controllable. Thus the moving plate yields a rotational self-motion. The attached video clip demonstrates such self-motion.

Case 5) When there are two pairs of two intersecting lines of $[A_f]$ as shown in Fig. 9(e), the dimension of variety for those four lines degenerates to three: the rotational motion of the mechanism cannot be controlled about the axis (line) connecting those two intersection points. The attached video clip demonstrates a resulting self-motion.

Case 6) When the upper four lines are parallel as shown in Fig. 9(f), singularity occurs. In this configuration, no rotational motion about the axis parallel to those lines can be controlled.

Case 7) When the upper four lines of $[A_f]$ lie on quadric surface (i.e., they all belong to a regulus), the dimension of variety degenerates to 3. An exemplary configuration belonging to this case is shown in Fig. 9(g).

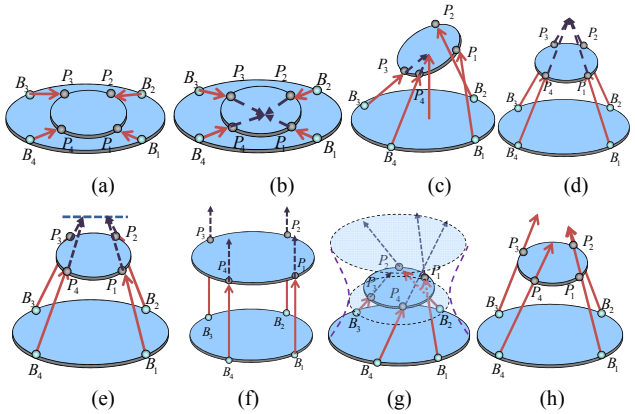

Fig. 9. Singular and non-singular configurations. (a) Case 1. (b) Case 2. (c) Case 3. (d) Case 4. (e) Case 5. (f) Case 6. (g) Case 7. (h) Non-singular case.

Now, result of the above singularity analysis will be taken into account for singularity-free design of the proposed mechanism. It can be seen that singularities from both case 1 and case 2 occur outside of workspace since the lowest positions of four input prismatic joints are set as shown in Table I. Thus, those two cases are not taken into account. However, singularities of case 4, case 5, and case 7 are related to the design parameters and they tend to appear around the center of workspace for the mechanism with symmetrical design parameters in general. To minimize the chance of these singularities, asymmetrical arrangement of contact points on the top plate is helpful as discussed in section III.

Fig. 9(h) shows the selected design in which an offset angle on the top plate ($\mu_b = 30^\circ$) is adopted to remove singularities within the workspace. Fig. 10 shows the singularity locus of this case on the $\alpha-\beta$ plane for fixed values of $z=0.07m$ and $\gamma=0^o$. It can be seen clearly from the figure that within the desired workspace $(-30^\circ\le\alpha,\beta\le30^\circ)$, this mechanism does not have any singularity even for different roll angles up to $\pm30^\circ$.

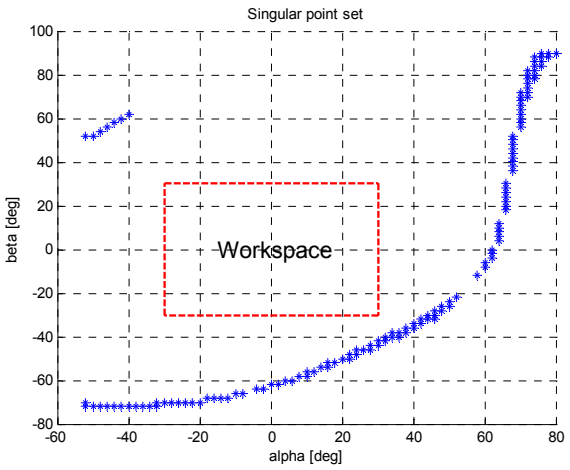

Fig. 10. Singularity locus and workspace with respect to α and β .

V. IMPLEMENTATION

In this section, we implement the 4-DOF parallel mechanism as a needle insertion device. Fig. 11 shows the proto type of the 4-DOF needle insertion device. As addressed, the mechanism has 3-DOF rotational motion and 1-DOF needle insertion motion. Particularly, Fig. 11(b) shows a fixed insertion point about which the remote center of motion (RCM) of the device is achieved in the steering motion stage. The mechanism consists of four active prismatic joints in the outer chains and a needle path guider in the middle chain. The active prismatic joint is designed to exhibit a linear motion by using a ball spline with stroke of 58mm and it is driven by a DC motor with a gear ratio of 14:1. The pitch of the ball spline is 0.4mm.

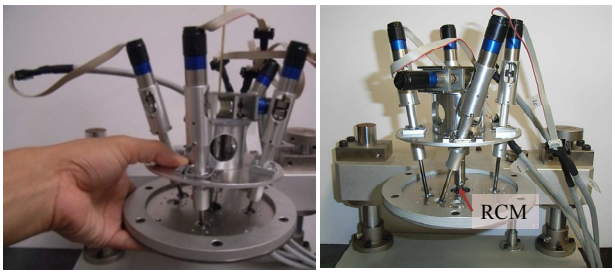

(a) (b)

Fig. 11. Needle insertion mechanism. (a) Mechanism. (b) Insertion point with RCM.

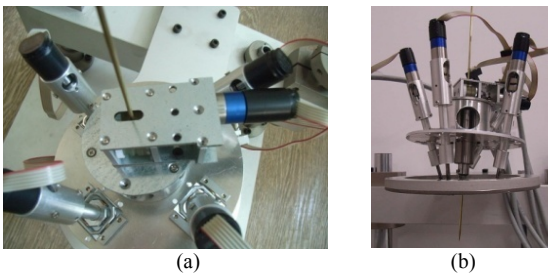

(a) (b)

Fig. 12. A 1-DOF automatic insertion device. (a) Top view. (b) Side view.

In addition, it is noted that the proposed mechanism of Fig. 11 has a limited stroke for the needle insertion operation due to its parallel structure. Thus, an optional (additional) 1-DOF translational motion device is designed and mounted on the top plate as shown in Fig. 12. This 1-DOF automatic needle insertion device could extend the range of the needle inserting motion enough to create a long stroke required for the needle insertion task. Table II and III show the specifications for the implemented device.

A needle can be inserted from the center of the upper plate as shown in Fig. 12(a) and goes through the path guider (the hole) which denotes the middle chain, and exits through the ball joint located at the center of the base plate. Note that through this path guider, the needle can be passively inserted by the user or be inserted by an 1-DOF automatic insertion device.

TABLE II
SPECIFICATION OF THE NEEDLE INSERTION DEVICE

Size	φ72x40xφ90 mm
Weight	868g
Motor model	DC-Micromotors 1717SR
Stroke	58mm
Tilting angle	±30°
Torsional angle	±30°
Resolution of prismatic joint	1μm

TABLE III
SPECIFICATION OF THE MOTOR: 1717SR

Size	Φ17x38.1 mm
Weight	41g
Gear ratio	14:1
Voltage	12 V
Speed up to	10000 rpm
Torque up to	2 mNm
Resolution of encoder	512 pulse
Drive	MCDC 3006S

Now, the needle insertion process using the implemented mechanism is explained. Initially, fix the top platform of this device to the target position of skin or body. Secondly, steer the mechanism so that the needle is oriented to the target direction. Thirdly, compress the whole mechanism so that the needle can be inserted into the skin. Fig. 13 shows such procedures. Note that the operating range of both steering (or tilting) and roll angles of this device is ±30° by taking into account the mechanical limit of spherical joints and mechanical interference. However, the roll angle of the needle can be controlled manually by the user's hand.

Figure 14 shows the control block diagram for our experimental system. Actuators are driven by a PID controller. A D/A (Digital-to-Analog) conversion are embedded in a motion board. Thus, a DC servo motor is controlled by this output voltage from the D/A converter, which corresponds to the magnitude of the joint error between the desired joint displacement and the current joint displacement.

The attached video clip demonstrates the whole needle insertion process. Through these demonstrations, it can be strongly contended that the implemented 4-DOF needle insertion parallel mechanism would be adequate in conducting various kinds of needle insertion tasks required in many different surgical procedures.

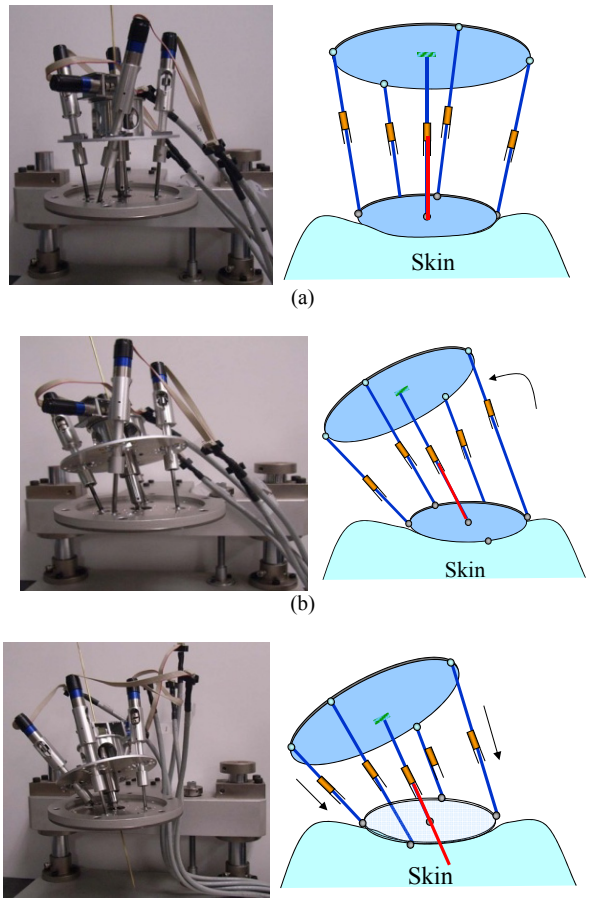

Fig. 13. Needle insertion procedure. (a) Fixation of the upper platform of the device to the target position of skin or body. (b) Steering the mechanism so that the needle is oriented to the target. (c) Compression of the whole mechanism so that the needle can be inserted into the skin.

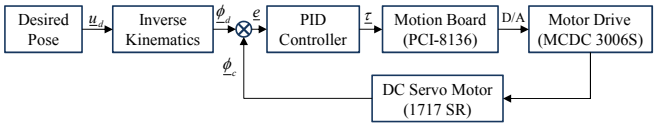

Fig. 14. Control block diagram.

VI. Conclusion

A new 4-DOF parallel mechanism having 3 rotations and one needle insertion motion was proposed and analyzed. Fundamental kinematic modeling and singularity analysis of this mechanism were conducted. The kinematic characteristics were analyzed in terms of two kinematic indices. Based on this result, a singularity-free design was proposed and an actual proto type needle insertion device was developed and tested to corroborate the working principle of this device for practical applications.

References

[1] D. Zlantanov and C. M. Gosselin, "A new parallel architecture with four degree of freedom," in *Proc. The 2nd workshop on Computational Kinematics*, 2001, pp.57-66.

[2] O. Company, F. Marquet, and F. Pierrot, "A new high-speed 4-DOF parallel robot synthesis and modeling issues," *IEEE Trans. Robot. Autom.*, vol. 19, no. 3, pp. 411-420, 2003.

[3] H. B. Choi, O. Company, F. Pierrot, A. Konno, T. Shibukawa, and M. Uchiyama, "Design and control of a novel 4-DOFs parallel robot H4," in *Proc. Int. Conf. Robot. Autom.*, 2003, pp.1183-1190.

[4] D. Chablat and P. Wenger, "A new concept of modular parallel mechanism for machining applications," in *Proc. Int. Conf. Robot. Autom.*, 2003, pp.3965-3970.

[5] Y. Fang and L.-W. Tsai, "Structure synthesis of a class of 4-DOF and 5-DOF parallel manipulators with identical limb structures," *Int. J. Robot. Res.*, vol. 21, no. 9, pp. 799-810, 2002.

[6] Z. Huang and Q. C. Li, "Type synthesis of symmetrical lower-mobility parallel mechanisms using the constraint-synthesis method," *Int. J. Robot. Res.*, vol. 22, no. 1, pp. 59-79, 2003.

[7] Q. C. Li and Z. Huang, "Mobility analysis of a novel 3-5R parallel mechanism family," *J. Mech. Design*, vol. 126, no. 1, pp. 79-82, 2004.

[8] Q. C. Li and Z. Huang, "A family of symmetrical lower-mobility parallel mechanisms with spherical and parallel subchains," *J. Robot. Syst.,* vol. 20, no. 6, pp-297-305, 2003.

[9] Y. Fang and L.-W. Tsai, "Structure synthesis of a class of 4-DOF and 5-DOF parallel manipulators with identical limb structures," *Int. J. Robot. Res*., vol. 21, no. 9, pp. 799–810, Sep, 2002.

[10] X. Kong and C. M. Gosselin, "Type synthesis of 3T1R 4-DOF parallel manipulators based on screw theory," *IEEE Trans. Robot. Auto*., vol. 20, no. 2, pp. 181–190, Apr. 2004.

[11] F. Gao, W. Li, X. Zhao, A. Jin, and H. Zhao, "New kinematic structures for 2-, 3-, 4-, and 5-DOF parallel manipulator designs," Mechanism and machine theory, vol. 37, 2002, 1395-1411.

[12] T. K. Podder, et al. "Evaluation of robotic needle insertion in conjunction with in vivo manual insertion in the operating room," in *Proc. IEEE Int. Workshop Robots Human Interactive Commu.*, 2005, pp. 66-72.

[13] S. P. DiMaio and S. E. Salcudean, "Simulated interface needle insertion," in *Proc.10th Symp. Haptic Interfaces for Virtual Envir. & Teleoperator Systm.*, 2002.

[14] C. M. Schneider, A. M. Okamura, and G. Fichtinger, "A robotic system for transrectal needle insertion into the prostate with integrated ultrasound," in *Proc. Int. Conf. Robot. Autom.*, 2004, pp.365-370.

[15] G. Fichtinger, J. Fience, C. Kennedy, I. Iordachita, G. Kronreif, D. Y. Song, E. C. Burdette, and P. Kazanzides, "Robotic assistance for ultrasound guided prostate brachytherapy," *Med. Image Anal*., vol. 12, no. 5, pp. 535-545, 2009.

[16] K. Masamune, G. Fichtinger, A. Patriciu, R. C. Susil, R. H. Taylor, L. R. Kavoussi, J. H. Anderson, I. Sakuma, T. Dohi, and D. Stoianovici, "System for robotically assisted percutaneous procedures with computed tomography guidance," *J. Comput. Aided Surg*., vol. 6, no. 6, pp. 370-383, 2001.

[17] On line: http://www.intuitivesurgical.com.

[18] C. Gosselin and J. Angels, "Singularity analysis of closed-loop kinematics chains," *IEEE Trans. Robot. Autom*., vol. 6, no. 3, pp. 281-290, 1991.

[19] J.-P. Merlet, *Parallel Robots*, Kluwer Academic Publishers, 2000.

[20] F. Hao and J. M. McCarthy, "Conditions for line-based singularities in spatial platform manipulators," *J. Robot. Syst*., vol. 15, no. 1, pp. 43-55, 1998.